

Article

Applied Potential Effect on $\text{ZnFe}_2\text{O}_4\text{-Fe}_2\text{O}_3$ Heterostructure for Generation of Photocurrents under Irradiation

I. Neelakanta Reddy ¹, Veeranjaneya Reddy Lebaka ², Suresh V. Chinni ^{3,4} , Ramachawolran Gobinath ^{5,*} , Jaesool Shim ^{1,*} and Cheolho Bai ¹

¹ School of Mechanical Engineering, Yeungnam University, Gyeongsan 38544, Republic of Korea

² Department of Microbiology, Yogi Vemana University, Kadapa 516005, India

³ Department of Biochemistry, Faculty of Medicine, Bioscience and Nursing, MAHSA University, Jenjarom 42610, Selangor, Malaysia

⁴ Department of Periodontics, Saveetha Dental College and Hospitals, Saveetha Institute of Medical and Technical Sciences, Chennai 600 077, India

⁵ Department of Foundation, RCSI & UCD Malaysia Campus, George Town 10450, Pulau Pinang, Malaysia

* Correspondence: r.gobinath@rcsiucd.edu.my (R.G.); jshim@ynu.ac.kr (J.S.)

Abstract: In this study, the performance of $\text{ZnFe}_2\text{O}_4\text{-Fe}_2\text{O}_3$ heterostructure was tested for photocurrent generation via photoelectrochemical activity under irradiation. Additionally, the effect of heterostructure photoanode on the structural, optical properties, and charge kinetic behavior of the photoelectrode was investigated. A combination of $\text{ZnFe}_2\text{O}_4\text{-Fe}_2\text{O}_3$ nanostructures exhibited an enhanced ability of light absorption compared to that of pristine Fe_2O_3 and ZnFe_2O_4 samples. For $\text{ZnFe}_2\text{O}_4\text{-Fe}_2\text{O}_3$ nanostructures, an electron–hole transfer resistance of 9.41 k Ω was achieved in a 0.1 M KOH electrolyte under irradiation, which is much lower than that of achieved values of pure Fe_2O_3 and ZnFe_2O_4 nanostructures. The generation of photocurrent density of $\text{ZnFe}_2\text{O}_4\text{-Fe}_2\text{O}_3$ photoanode considerably increased in 0.1 M KOH electrolytes under irradiation compared to those of the other samples due to the greater active sites, electronic band structure, absorption capability of photoanode, and considerable improvements in the charge transfer resistance, limiting current density, exchange current density, and Tafel slope. Further, the applied potential showed a strong significant influence on the generation of photocurrent for the synthesized photoelectrodes. At 0.5 V applied potential, the heterostructure showed a maximum and enhanced current density compared to pristine samples. Thus, $\text{ZnFe}_2\text{O}_4\text{-Fe}_2\text{O}_3$ photoanodes were established to be beneficial and stable nanostructures for photoelectrochemical water splitting.

Keywords: heterostructure; photocurrents; applied potentials; water splitting; resistance



Citation: Reddy, I.N.; Lebaka, V.R.; Chinni, S.V.; Gobinath, R.; Shim, J.; Bai, C. Applied Potential Effect on $\text{ZnFe}_2\text{O}_4\text{-Fe}_2\text{O}_3$ Heterostructure for Generation of Photocurrents under Irradiation. *Crystals* **2022**, *12*, 1726. <https://doi.org/10.3390/cryst12121726>

Academic Editor: Igor Neri

Received: 13 October 2022

Accepted: 19 November 2022

Published: 28 November 2022

Publisher's Note: MDPI stays neutral with regard to jurisdictional claims in published maps and institutional affiliations.



Copyright: © 2022 by the authors. Licensee MDPI, Basel, Switzerland. This article is an open access article distributed under the terms and conditions of the Creative Commons Attribution (CC BY) license (<https://creativecommons.org/licenses/by/4.0/>).

1. Introduction

Presently, the utilization of hydrocarbon-based fuels in various sectors generating unlimited pollutants causes damage to the earth's environment. An alternative eco-friendly energy source is needed urgently to prevent or reduce the pollutant emissions. In this process, the most popular photoelectrochemical activity (PA) is a highly considerable alternative technique to produce environmental fuel like hydrogen. In the PA technique, semiconductors are used as catalyst materials for fuel generators under the irradiation of solar light. Numerous semiconducting nanostructures were tested for PA such as IrO_x , $\text{TM}_3\text{C}_{12}\text{O}_{12}$, Ni_3Se_4 , TiO_2 , etc. [1–4]. However, the mono-nanostructures could have the ability to generate induced currents due to less optical utilization, a high recombination rate, and poor kinetics. To overcome the limitation of the catalyst materials, several techniques were adopted to improve the catalyst activity of the catalysts, for example, doping, development of heterostructures, and alteration of morphology.

Nowadays, the spinel structures of AB_2X_4 , where A and B can be divalent and trivalent, are used as a photocatalyst due to their excellent physical and chemical properties.

In the spinal structures, the ZnFe_2O_4 nanostructures are well-established for catalytic applications [5] owing to the band gap, electrochemical stability, and availability. However, the main catalytic activity is limited because of its spectral response range, poor conductivity, fast recombination rate, and poor electronic and separation behavior. Therefore, the researchers focused on increasing the charge transfer and separation rate by constructing heterostructures, loading co-catalysts, and doping. The development of heterostructures could exhibit several advantages and could enhance the charge movement at the solid–liquid junction, the photon harvesting range, the excitation of electron and hole, and the surface reactions.

The Fe_2O_3 nanostructures were utilized in the study to develop a heterostructure photocatalyst due to its high estimated efficiency, stability, availability, and narrow optical band gaps. Additionally, the Fe_2O_3 nanostructures, with the combination of other semiconducting nanostructures, can significantly enhance catalytic properties under illumination [6]. Further, the band edge locations of ZnFe_2O_4 are preferably offset from that of Fe_2O_3 , and it is assumed that the ZnFe_2O_4 - Fe_2O_3 heterostructures can efficiently enrich the charge separation produced in both ZnFe_2O_4 and Fe_2O_3 regions by permitting movement of charges. Because the ZnFe_2O_4 valence band edge is positioned towards a more negative voltage compared to Fe_2O_3 , the ZnFe_2O_4 - Fe_2O_3 anode that may be best employed is the band edge offset to generate charge in the Fe_2O_3 and transfer to the ZnFe_2O_4 , which then moved to the catalyst/electrolyte interface. This should be extremely beneficial for photon-harvesting the extra charge produced in Fe_2O_3 . The charges produced in the ZnFe_2O_4 can transfer to the Fe_2O_3 and then move to the electrode contact.

In the study, the preparation, analysis, and photoelectrochemical properties of ZnFe_2O_4 - Fe_2O_3 heterostructure were systematically investigated, achieving an enhanced light absorption and highest photocurrent generation in ZnFe_2O_4 - Fe_2O_3 heterostructure.

2. Materials and Methods

2.1. ZnFe_2O_4 Nanoparticles

The precipitation method was utilized to prepare ZnFe_2O_4 nanostructures. Firstly, 0.26 g of iron (III) chloride hexahydrate and 0.28 g of zinc nitrate hexahydrate were poured separately into 90 mL of H_2O and continuously stirred for 60 min to achieve a uniform solution, respectively. The iron source solution was slowly added to the zinc source solution and stirred for 30 min. Then, the solution pH was adjusted to 12 with 0.1 M NaOH solution and maintained at a temperature of 82 °C for 180 min until the precipitate occurred. The room temperature that attained the final solution was cleaned with H_2O and ethanol several times via centrifugation and dried at 60 °C for 22 h.

2.2. Fe_2O_3 Nanoparticles

Fe_2O_3 nanoparticles were synthesized by hydrothermal method. Initially, 0.4 g of iron (II) chloride tetrahydrate was added to 40 mL of H_2O and continuously stirred for 60 min to attain a completely dissolved solution. The solution pH was adjusted to 10 with an NH_4OH solution and continued to stir for 50 min. The final solution was poured into a 150 mL Teflon-lined autoclave and heated at 180 °C for 240 min. The room temperature attained solution was cleaned with H_2O and ethanol several times via centrifugation and dried at 80 °C for 14 h. The dried Fe_2O_3 powders were post-annealed at 500 °C for 2 h.

2.3. ZnFe_2O_4 - Fe_2O_3 Heterostructures

The equal weights of each pristine sample of ZnFe_2O_4 and Fe_2O_3 were ground together for 60 min with a mortar and pestle. Then, the collected powder was poured into an alumina boat and kept at 500 °C for 4 h in a muffle furnace. The schematic of the preparation of the composite structure is given Figure 1.

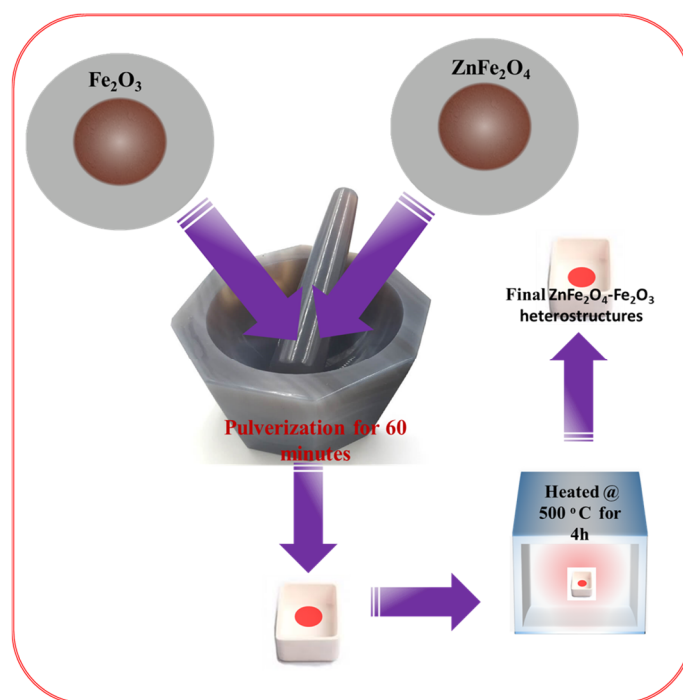


Figure 1. The schematic of the preparation of the composite structure.

2.4. Photoelectrodes Fabrication

Each 2 mg of synthesized ZnFe_2O_4 (Z), Fe_2O_3 (F), and $\text{ZnFe}_2\text{O}_4\text{-Fe}_2\text{O}_3$ (ZF) nanostructures were individually poured into 4 mL of ethylene glycol and probe-sonicated for 2 min to achieve a uniform dispersed solution for drop-casting. These solutions were drop-casted in 1 cm^2 at $140\text{ }^\circ\text{C}$ on cleaned ITO-coated glass substrates of $2 \times 1\text{ cm}^2$ and then transferred to a vacuum oven for drying, kept at $80\text{ }^\circ\text{C}$ for 48 h. Before coating the glass substrates, the substrates were cleaned with water and isopropyl alcohol several times in each solution via ultrasonication. These fabricated electrodes were utilized for electrochemical and impedance analysis in 0.1 M KOH electrolyte and studied various photoelectrochemical water splitting parameters such as potentiodynamic electrochemical impedance spectroscopy (PEIS), linear sweep voltammetry (LSV), chronoamperometry (CA), and Tafel plots under dark and light conditions, respectively.

2.5. Characterization

The synthesized samples were characterized with X-ray diffraction (PANalytical X'pert PRO, The Netherlands), scanning electron microscopy (SEM, Hitachi S-4800, Tokyo, Japan), high-resolution transmission electron microscopy (HRTEM, G2 F30 S-Twin), UV-Vis spectroscopy (Neogen NEO-D3117, Seoul, South Korea), and X-ray photoelectron spectroscopy (XPS, Thermo Fisher Scientific MultiLab 2000, Seoul, South Korea) to investigate the crystalline phase, morphology, optical properties, and chemical states.

2.6. Electrochemical Studies

The synthesized samples were tested with potentiodynamic electrochemical impedance analyses (PEIS), linear sweep voltammetry (LSV), chronoamperometry (CA), and Tafel analyses (T), under the dark and light conditions in the 0.1 M KOH aqueous electrolyte using a three-electrode (Pt: counter; Ag/AgCl: reference; WE: working electrode) BioLogic potentiostat (SP-200, France). All the fabricated electrodes were illuminated with 100 mW cm^{-2} of the light source (ABET Technologies Inc., Model 10500, Milford, CT, USA). The impedance analysis of the synthesized electrodes was performed in the applied frequency range of 7 MHz to 1 Hz at an amplitude of 10 mV under a dark/light state in 0.1 M KOH electrolyte.

3. Results and Discussion

The crystalline structure of synthesized ZnFe_2O_4 (Z), Fe_2O_3 (F), and $\text{ZnFe}_2\text{O}_4\text{-Fe}_2\text{O}_3$ (ZF) nanostructures are shown in Figure 2. Figure 2 shows an XRD analysis of Z nanostructures, observing a cubic crystalline structure as per JCPDF card No.:89-4926 with the space group of Fd-3m. The reflected peak positions were noticed at 18.1° , 29.9° , 35.3° , 37.0° , 42.8° , 53.2° , 56.7° , 62.2° , and 73.5° with a (h l k) planes of (111), (220), (311), (222), (400), (422), (511), (440), and (533), demonstrating an efficient synthesis of Z nanostructures without any other impurities [7]. The phase analysis of F nanostructures, shown in Figure 2, specifies a rhombohedral crystalline structure as per JCPDF card No.:79-0007 with the space group of R-3c. The characteristic peaks of F were noticed at 24.2° , 33.2° , 35.7° , 40.9° , 49.6° , 54.1° , 57.7° , 62.5° , 64.1° , 72.0° , and 75.5° with a (h l k) planes of (012), (104), (110), (113), (024), (116), (122), (214), (300), (1010), and (220) representing an efficacious preparation of F nanostructures without any other impurities [8]. Further, the ZF heterostructure shows a combination of XRD peaks in pristine Z and F samples, demonstrating the same crystalline structure with strong interaction among the structures, as shown in Figure 2. No impurities were noticed during the formation of heterostructures, which signifies the quality of the synthesized samples. This strong interaction that occurred in the heterostructure may improve the charge carrier mechanisms, which are more beneficial for achieving enhanced current densities.

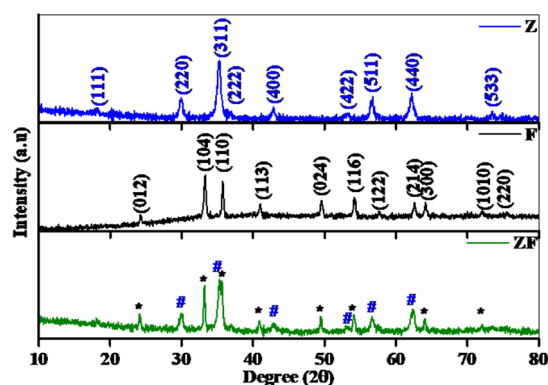


Figure 2. Phase analysis of ZnFe_2O_4 (Z), Fe_2O_3 (F), and $\text{ZnFe}_2\text{O}_4\text{-Fe}_2\text{O}_3$ (ZF) nanostructures.

SEM analysis of synthesized ZnFe_2O_4 (Z), Fe_2O_3 (F), and $\text{ZnFe}_2\text{O}_4\text{-Fe}_2\text{O}_3$ (ZF) nanostructures were shown in Figure 3. Figure 3a shows an irregular sizes of nanoparticles nanostructure of Z samples, with the particle sizes ranging from ~ 14 nm to 35 nm, respectively.

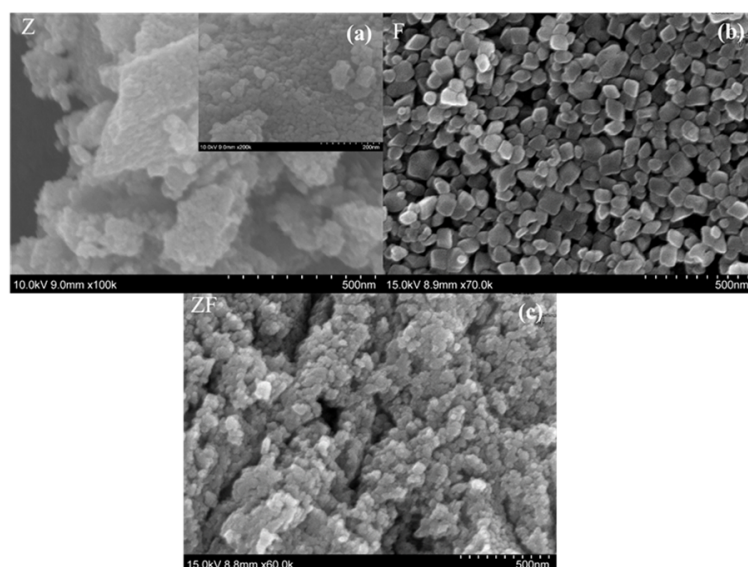


Figure 3. Morphology images of (a) ZnFe_2O_4 (Z), (b) Fe_2O_3 (F), and (c) $\text{ZnFe}_2\text{O}_4\text{-Fe}_2\text{O}_3$ (ZF) nanostructures.

The morphology of synthesized F samples shown in Figure 3b shows an irregular shape of nanoparticles nanostructure. ZF heterostructure shows similar morphology to pristine samples with strong interaction among the Z and F nanostructures, as shown in Figure 3c. In addition, to investigate the more detailed morphology of synthesized ZF heterostructure, the HR-TEM analysis was performed (Figure 4a–c). Figure 4a,b shows a clear strong interaction among the pristine Z and F samples with a lattice fringe width of 0.489 nm and 0.252 nm. The selected area electron diffraction pattern of the ZF sample, shown in Figure 4c, observed a ring pattern with the combination of Z and F nanostructures. These high-resolution morphology analyses agree well with the SEM and XRD analyses.

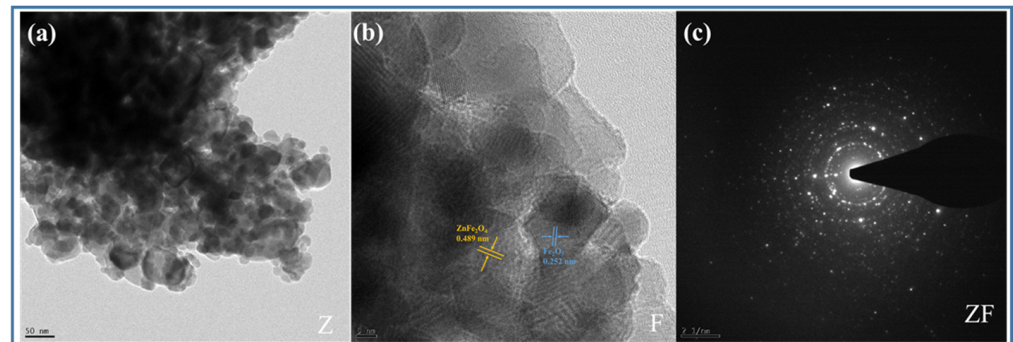


Figure 4. High resolution morphology images of $\text{ZnFe}_2\text{O}_4\text{-Fe}_2\text{O}_3$ (ZF) nanostructures.

The optical bandgap of the synthesized ZnFe_2O_4 (Z), Fe_2O_3 (F), and $\text{ZnFe}_2\text{O}_4\text{-Fe}_2\text{O}_3$ (ZF) nanostructures were shown in Figure 5a. The estimated optical bandgap of 2.05, 1.97, and 2.01 eV was achieved for Z, F, and ZF nanostructures. These obtained bandgap values are well-matched with the reported literature [9,10]. The ZF structures changing the bandgap may be due to alteration of sizes and oxygen vacancies. Additionally, the ZF bandgap changes are due to the alteration of heterostructure band edges due to the static electric field-induced potential energy and strain-induced deformation potential.

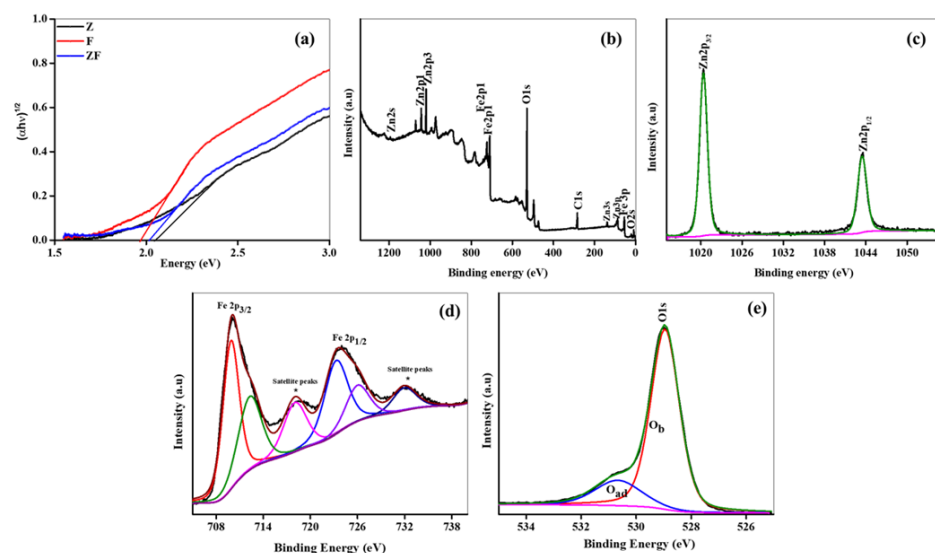


Figure 5. Optical properties of (a) bandgap plots, (b) XPS survey spectra of $\text{ZnFe}_2\text{O}_4\text{-Fe}_2\text{O}_3$ (ZF) nanostructures, (c) $\text{Zn}2p$ spectra, (d) $\text{Fe}2p$ spectra, and (e) $\text{O}1s$ spectra.

The XPS analysis of ZF nanostructures was shown in Figure 5b–e. The XPS survey spectra consists only of the synthesized heterostructure elemental peaks, which indicates the purity of the nanostructures, as represented in Figure 5b. Further, to investigate the electronic states of the heterostructure, the core-level peaks were recorded, as shown in

Figure 5c–e. For ZF nanostructures, the deconvoluted peaks of Zn2p showed spin-orbit split peaks with a distance of ~ 23.1 eV and binding energies of ~ 1020.3 and ~ 1043.4 eV, ascribed to the Zn2p_{1/2} and Zn2p_{3/2} states of Zn²⁺ in the ZF nanostructures (Figure 5c). The deconvoluted Fe2p peaks of ZF nanostructures were shown in Figure 5d, with binding energies positioned at 709.9, 712.3, 718.1, 723.3, 726.1, and 731.9 eV, allotted to Fe2p_{3/2}, Fe2p_{1/2}, and satellite peaks of Fe³⁺. Further, the O1s peaks of ZF nanostructures are shown in Figure 5e and the energy peaks are located at 528.9 and 530.6 eV, which are attributed to the bonded lattice oxygen and adsorbed oxygen.

The impedance analysis of the synthesized samples was performed to understand the charge transfer behavior under the dark and light conditions in 0.1 M KOH aqueous electrolyte. The recorded Nyquist plots for ZnFe₂O₄ (Z), Fe₂O₃ (F), and ZnFe₂O₄-Fe₂O₃ (ZF) nanostructures under light ON/OFF states in 0.1 M KOH electrolyte were shown in Figure 6. In general, the Nyquist plots exhibit three regions: (1) contact resistance region at the lower applied frequency, (2) charge kinetics region at the mid of the applied frequency, and (3) diffusion region at the higher applied frequency (Figure 6a). Herein, the recorded Nyquist plots for Z, F, and ZF nanostructures exhibited three regions under both the dark and light state at the applied frequency range of 7 MHz to 1 Hz (Figure 6b). The radius of the semicircle in the charge kinetics region varied for all the photoelectrodes under dark and light states. However, in the light state, the radius of the semicircle is significantly smaller than that of the dark state for all the electrodes in 0.1 M KOH, demonstrating that the fabricated electrodes respond well to the incident light in the three-electrode setup. The smallest radius of the semicircle was noticed for the ZF electrode than that of other Z and F electrodes, indicating that the ZF electrode may exhibit a better charge transfer mechanism and could generate enhanced photocurrents under illumination. To explore this in detail, the recorded Nyquist plots were fitted with the physical equivalent circuit, and the fitted circuit for all the prepared electrodes is shown in the inset of Figure 6b. The circuit consists of R1, R2, R3, C1, and C3, referring to a resistance due to the interface of 0.1 M KOH electrolyte and the electrode surface, bulk catalyst charge-transport resistance, charge-transfer resistance, bulk catalyst capacitance, and Helmholtz capacitance, as given in Table 1. The R1 values should be lower for attaining good charge transportation among the surface of the fabricated electrode and the chosen electrolyte to achieve higher photocurrents via photoelectrochemical activity. In the light state, the synthesized electrodes showed lower solution resistance values than that in the dark state. The lowest R1 value of 16.92 Ω was observed under a light state for ZF heterostructures than that of other electrodes in both dark and light states, signifying that the ZF nanostructures have good contact with the electrolyte at the interface of the fabricated electrode surface and the KOH aqueous electrolyte, which may increase the charge carriers' movement at the solid–liquid interface. Additionally, this allows charge carriers into electrolytes for the further catalytic process without accumulating at the junction. The R2 values of the synthesized electrodes showed a lower resistance in the light state than that in the dark state. The lowest value of 22.98 Ω was achieved for the ZF electrode under a light state compared with Z and F electrodes, indicating that the ZF electrode exhibits minimized grain boundaries and effective charge separation [11]. The charge transfer resistance of the synthesized electrodes showed a lower light state than that of the dark state, which can be observed in Table 1. The ZF heterostructures showed the lowest R3 value of 9.41 k Ω under the light state than that of other Z and F electrodes, which signifies that the ZF has a good transfer mechanism and may be beneficial for getting a higher catalytic activity under illumination conditions. The capacitance values of the synthesized Z, F, and ZF electrodes were higher in the light state than that in the dark state. The ZF nanostructures showed a maximum C1 value of 8.06 nF compared to Z and F photoelectrodes, due to the formation of the heterostructure that evaded charge buildup at the solid–liquid interface. The Helmholtz capacitance values of the synthesized photoanodes specified the charge transfer capacity of the electrode surface to the KOH electrolyte solution. The higher C3 value of 6.87 μ F for ZF heterostructure under light state compared to Z and F anodes indicates a larger charge carrier buildup at

the ZF surface/0.1 M KOH interface than at the Z and F anodes [12]. Therefore, the above analysis suggests that the ZF heterostructure anode can generate improved photocurrents under illumination in the 0.1 M KOH. Additionally, under dark and light states, the Bode and phase plots were recorded for Z, F, and ZF electrodes in 0.1 M KOH electrolyte, as shown in Figure 6c,d. The ZF heterostructures showed a shifted impedance toward the low frequencies compared with the Z and F samples, which may be associated with the rapid generation and improved charge carriers' transportation. This improvement was equitable for decreasing the recombination rate in heterostructures [13]. Figure 6d shows a Bode phase analysis of Z, F, and ZF anodes under both conditions in 0.1 M KOH. The ZF heterostructure showed a shifted frequency peak towards a smaller value, which advised a superior lifetime of charges than that of Z and F anodes. This designated that the uniform distribution of catalysts enhances the charge separation and improves the charge lifetime [14].

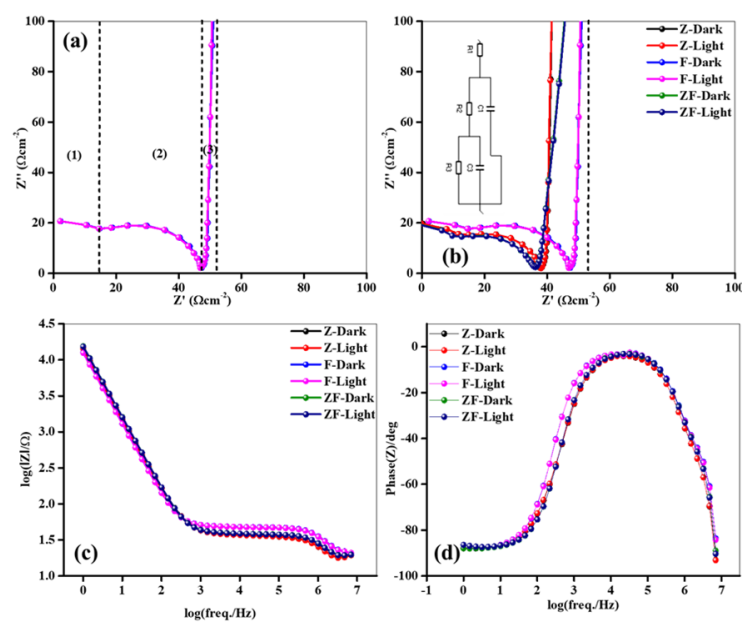


Figure 6. (a) Nyquist plots with general specified regions, (b) Nyquist plots of ZnFe_2O_4 (Z), Fe_2O_3 (F), and $\text{ZnFe}_2\text{O}_4\text{-Fe}_2\text{O}_3$ (ZF) nanostructures under light ON/OFF states in 0.1 M KOH electrolyte, (c) bode plots of ZnFe_2O_4 (Z), Fe_2O_3 (F), and $\text{ZnFe}_2\text{O}_4\text{-Fe}_2\text{O}_3$ (ZF) nanostructures under light ON/OFF states in 0.1 M KOH electrolyte, and (d) phase plots of ZnFe_2O_4 (Z), Fe_2O_3 (F), and $\text{ZnFe}_2\text{O}_4\text{-Fe}_2\text{O}_3$ (ZF) nanostructures under light ON/OFF states in 0.1 M KOH electrolyte.

Table 1. Equivalent circuit fitted values of synthesized samples in 0.1 M KOH electrolyte under dark/light state.

Electrode	Condition	R1 (Ω)	R2 (Ω)	R3 (kΩ)	C1 (nF)	C3 (μF)
ZnFe_2O_4 (Z)	Dark	30.5	35.73	266.24	2.59	10.36
	Light	21.88	35.72	242.02	2.58	10.15
Fe_2O_3 (F)	Dark	34.4	46.19	251.11	1.79	12.2
	Light	23.02	46.08	238.37	1.76	12.12
$\text{ZnFe}_2\text{O}_4\text{-Fe}_2\text{O}_3$ (FZ)	Dark	24.76	26.27	10.99	9.84	7.71
	Light	16.92	22.98	9.41	8.06	6.87

Tafel plots of the fabricated Z, F, and ZF anodes were recorded to realize the hydrogen evolution mechanism in 0.1 M KOH aqueous electrolyte under dark and light conditions. The plotted Tafel data for the synthesized Z, F, and ZF anodes were presented in Figure 7. All the nanostructures exhibited a shift in voltage towards the anode under a light state

compared with the dark state. It signifies that the anodes produced a large number of charges, which significantly helps to improve the catalytic activity. Further, the Tafel plots of the anodes under the light ON/OFF conditions in the electrolyte were fitted to attain the Tafel slopes, limiting current density (J_L) and exchange current density (J_p) (Table 2). Usually, a smaller Tafel slope indicates that the anodes need less applied voltages to generate induced charges. The Tafel slopes achieved for the electrodes under the light states showed less than that of the dark state for the anodes. However, the lowest Tafel slopes of 58.8 mVdec^{-1} were achieved for the ZF anode, which is much smaller than that of Z and F anodes in any conditions, representing that the anode produced huge, induced charges, and hence, that the ZF anode has a fast charge kinetics [15]. The estimated J_L and J_p values of the anodes under dark and light states in 0.1 M KOH electrolytes are given in Table 2. The J_L values of the ZF anode showed a lower value compared to the Z and F anodes under the ON/OFF conditions. The lowest J_L and J_p of -0.04 and -1.70 mAcm^{-2} were achieved for ZF under the light ON condition, demonstrating that ZF offers more of a transfer rate. Hence, ZF may show improved catalytic activity under illumination.

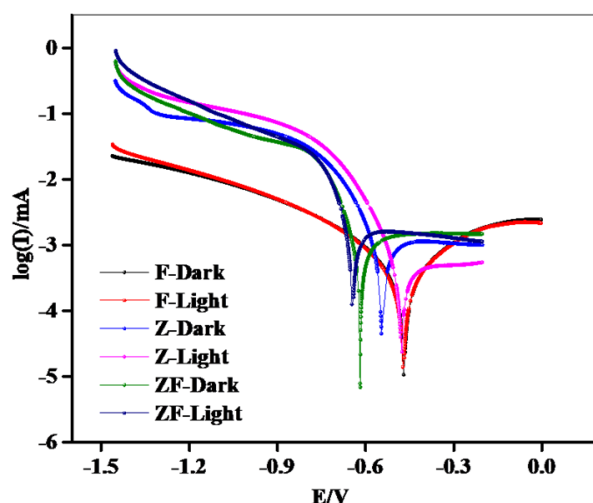


Figure 7. Tafel plots of ZnFe_2O_4 (Z), Fe_2O_3 (F), and $\text{ZnFe}_2\text{O}_4\text{-Fe}_2\text{O}_3$ (ZF) nanostructures under light ON/OFF states in 0.1 M KOH electrolyte.

Table 2. Tafel analysis of the synthesized anodes under light ON/OFF states in 0.1 M KOH electrolyte.

Electrolyte 0.1 M	Photoelectrode	Tafel Slopes		J_L		J_p	
		Dark mVdec^{-1}	Light mVdec^{-1}	Dark mAcm^{-2}	Light mAcm^{-2}	Dark mAcm^{-2}	Light mAcm^{-2}
KOH	ZnFe_2O_4 (Z)	82.9	76.9	-1.64	-1.46	-3.46	-3.25
	Fe_2O_3 (F)	90	82.8	-0.49	-0.24	-2.09	-2.01
	$\text{ZnFe}_2\text{O}_4\text{-Fe}_2\text{O}_3$ (ZF)	61.9	58.5	-0.22	-0.04	-1.72	-1.7

KOH electrolyte.

The sweep voltammetry analysis of Z, F, and ZF electrodes is shown in Figure 8a. A sharp increment in photocurrent was noticed from $\sim 0.6 \text{ V}$ to 1 V in the applied potential for all the electrodes under both the light/dark states. However, the photocurrents generated by the fabricated electrodes showed higher current densities in the light condition than that in the dark state. The pristine Z electrode generated almost null photo-induced currents under illumination. However, the heterostructured sample showed a significantly improved generation of photo-induced current densities compared to pristine Z and F samples. The maximum photo-induced current density of 2.41 mAcm^{-2} was observed for the ZF electrode under a light state due to lower solution resistance and charge transfer resistance. The obtained photoanode performance was compared with the reported literatures, given in Table 3.

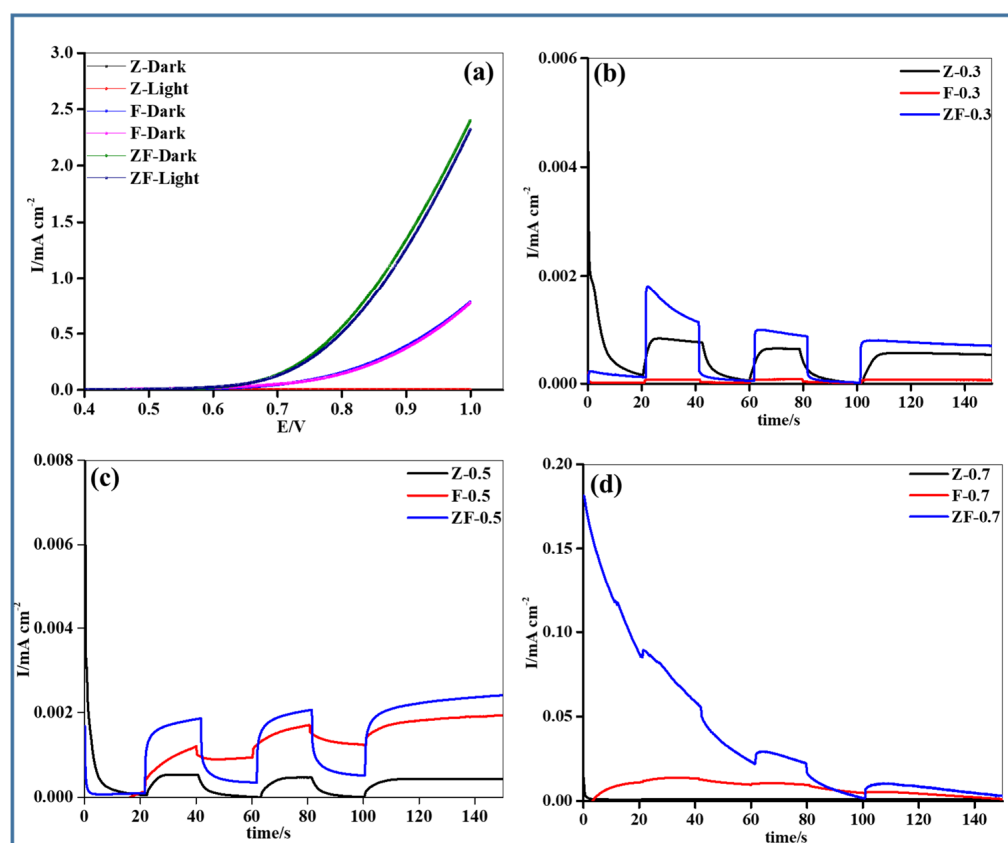


Figure 8. (a) Voltammetry analysis of ZnFe₂O₄ (Z), Fe₂O₃ (F), and ZnFe₂O₄-Fe₂O₃ (ZF) nanostructures under light ON/OFF states in 0.1 M KOH electrolyte, (b–d) chronoamperometry plots recorded at 0.3, 0.5, and 0.7 V in KOH electrolyte.

Table 3. Comparison of photoanode performance with reported literature.

Catalyst	Electrolyte	Current Density (mAcm ⁻²)	Reference
ZnO/ZnFe ₂ O ₄	0.1 M Na ₂ SO ₄	0.29	[16]
α-Fe ₂ O ₃ /CdS	1 M NaOH + 0.1 M Na ₂ S	0.6	[17]
Fe ₂ O ₃ /Ti:ZnFe ₂ O ₄	1 M NaOH	0.2	[18]
SrTiO ₃ /Fe ₂ O ₃	0.2 M Na ₂ SO ₄	0.052	[19]
WO ₃ /α-Fe ₂ O ₃	0.5 M Na ₂ SO ₄	0.84	[20]
ZnFe ₂ O ₄ /ZnO	0.1 M Na ₂ SO ₄	1.4	[21]
α-Fe ₂ O ₃ /ZnFe ₂ O ₄	1 M NaOH	0.1	[22]
Fe ₂ O ₃ /ZnFe ₂ O ₄	0.1 M KOH	2.41	Present work

CA analysis of the fabricated Z, F, and ZF anodes were examined at various applied potentials of 0.3, 0.5, and 0.5 V in 0.1 M KOH liquid electrolyte, as shown in Figure 8b–d. The synthesized Z, F, and ZF electrodes showed excellent switching behavior during light ON/OFF states. The applied potential has a significant effect on the generation of photocurrents under light conditions. The photocurrent generation increased with applied voltages up to 0.5 V and then decreased at a higher applied potential of 0.7 V. The maximum photocurrent density was shown at an applied voltage of 0.5 V for all the electrodes. However, the heterostructure of the ZF electrode showed the highest current densities in all the applied voltages compared to that of the Z and F electrodes. This could be due to the construction of heterostructures with a combination of Z and F, decreased resistance values, improved active sites, transfer kinetics, lower recombination rate, and increased capacitance behavior. Therefore, the ZF heterostructure generated the highest

photocurrents at an applied voltage of 0.5 V when compared with the others under various conditions. The produced currents of Z, F, and ZF anodes at different applied voltages are as follows: $0.7\text{ V} < 0.5\text{ V} > 0.3\text{ V}$.

The photocurrent generation of the heterostructure is schematically represented in Figure 9. Under ON condition, the photoanode absorbs light energy in terms of photons, generates a cloud of electrons and holes on the photoanode surface, and further separation of charges occurs due to the variation of work functions. The positive charges move to the surface of the electrode and produces oxygen from the liquid electrolyte. At the same time, the generated negative charge carriers move towards the counter electrode and generate a hydrogen. Therefore, the heterostructure increases the light absorption ability due to the synergistic effect of the electrodes [23,24], thereby increasing the generation of charge pairs and enhancing the catalytic activity.

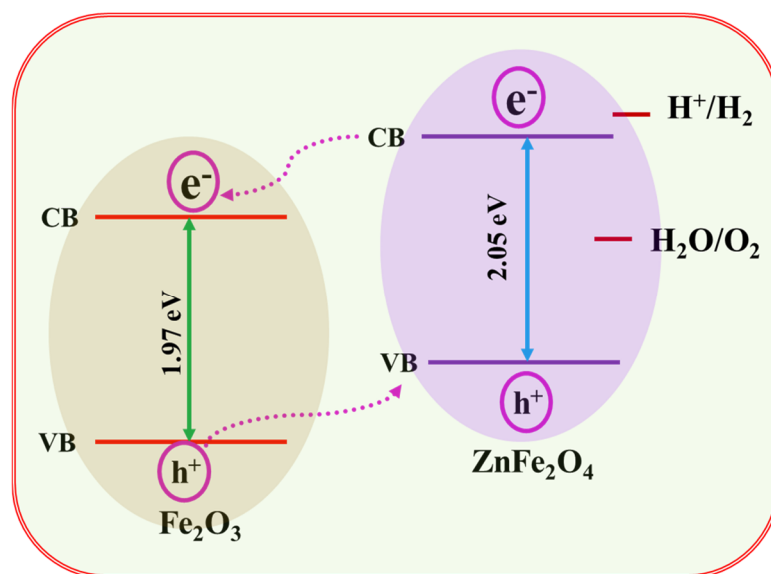


Figure 9. The schematic energy diagram of the heterostructure.

4. Conclusions

ZnFe₂O₄-Fe₂O₃ heterostructure was synthesized successfully via a facile method, observing a significant influence of heterostructure on the optical and catalytic properties. Additionally, we noticed that the ZnFe₂O₄-Fe₂O₃ heterostructure exhibited much better charge transfer, compatibility with electrolyte, and utilization of incident light. The lowest charge transfer resistance and electrolyte resistance of 9.41 kΩ and 16.92 Ω for ZnFe₂O₄-Fe₂O₃ heterostructure was under illumination. Further, the minimum Tafel slope of 58.5 mVdec⁻¹ was achieved for ZnFe₂O₄-Fe₂O₃ nanostructures. The highest photocurrents under irradiation were obtained for the ZnFe₂O₄-Fe₂O₃ sample could be due to the strong interaction and synergistic effect of nanostructures. Hence, the development of ZnFe₂O₄-Fe₂O₃ heterostructures can enhance the generation of photo-induced currents via photoelectrochemical activity using freely available visible light.

Author Contributions: I.N.R.: Data curation, Formal analysis, Investigation, Methodology, Writing—original draft, Conceptualization. V.R.L.: Conceptualization, Formal analysis. S.V.C.: Conceptualization, Funding acquisition, Formal analysis. R.G.: Conceptualization, Formal analysis. J.S.: Methodology, Project administration, Resources, Visualization. C.B.: Conceptualization, Methodology, Validation. All authors have read and agreed to the published version of the manuscript.

Funding: This work was supported by the National Research Foundation (NRF) of Korea under grant Nos. 2020R1A4A1019227 and 2020R1A2C1012439.

Data Availability Statement: Not applicable.

Conflicts of Interest: The authors declare no conflict of interest.

References

1. Altowyan, A.S.; Mohamed, S.; Khaled, A.; Adel, M.E.S. The Influence of Electrode Thickness on the Structure and Water Splitting Performance of Iridium Oxide Nanostructured Films. *Nanomaterials* **2022**, *12*, 3272. [[CrossRef](#)]
2. Quan, L.; Zhen, F.; Dianhui, W. Theoretical Study on the Electrochemical Water Splitting of Two-Dimensional Metal–Organic Frameworks $\text{TM}_3\text{C}_{12}\text{O}_{12}$ (TM = Mn, Fe, Co, Ni). *Crystals* **2022**, *12*, 1289.
3. Chuancang, Z.; Hongyu, W.; Feipeng, Z.; Yigao, M. Cobalt, Ferrum Co-Doped Ni_3Se_4 Nano-Flake Array: An Efficient Electrocatalyst for the Alkaline Hydrogen Evolution and Overall Water Splitting. *Crystals* **2022**, *12*, 666.
4. Soundarya, T.L.; Jayalakshmi, T.; Mabkhoot, A.A.; Mohammed, J.; Antonio, A.; Alharthi, F.A.; Naushad, A.; Nagaraju, G. Ionic Liquid-Aided Synthesis of Anatase TiO_2 Nanoparticles: Photocatalytic Water Splitting and Electrochemical Applications. *Crystals* **2022**, *12*, 1133. [[CrossRef](#)]
5. Sundaram, C.; Chris, B.; Peixin, Z.; Zheling, L.; Qiuhua, Y.; Xiangzhong, R.; Libo, D. Spinel photocatalysts for environmental remediation, hydrogen generation, CO_2 reduction and photoelectrochemical water splitting. *J. Mater. Chem. A* **2018**, *6*, 11078–11104.
6. Jeong, H.K.; Yong, C.; Jin, H.K.; Jaerim, K.; Young, K.K.; Jong, K.K.; Jae, S.L. ZnFe_2O_4 Dendrite/ SnO_2 Helix 3D Hetero-Structure Photoanodes for Enhanced Photoelectrochemical Water Splitting: Triple Functions of SnO_2 Nanohelix. *Small* **2021**, *17*, 2103861.
7. Li, L.; Bi, H.; Gai, S.; He, F.; Gao, P.; Dai, Y.; Zhang, X.; Yang, D.; Zhang, M.; Yang, P. Uniformly Dispersed ZnFe_2O_4 Nanoparticles on Nitrogen-Modified Graphene for High-Performance Supercapacitor as Electrode. *Sci. Rep.* **2017**, *7*, 43116. [[CrossRef](#)] [[PubMed](#)]
8. Hjiri, M. Highly Sensitive NO_2 Gas Sensor Based on Hematite Nanoparticles Synthesized By Sol–Gel Technique. *J. Mater. Sci. Mater. Electron.* **2020**, *31*, 5025–5031. [[CrossRef](#)]
9. Shaterian, M.; Rezvani, A.; Abbasian, A.R. Controlled synthesis and self-assembly of ZnFe_2O_4 nanoparticles into microspheres by solvothermal method. *Mater. Res. Express* **2019**, *6*, 1250–1255. [[CrossRef](#)]
10. Sharmila, M.; Mani, R.J.; Parvathiraja, C.; Kader, S.M.A.; Siddiqui, M.R.; Wabaidur, S.M.; Islam, M.A.; Lai, W.C. Photocatalytic Dye Degradation and Bio-Insights of Honey-Produced $\alpha\text{-Fe}_2\text{O}_3$ Nanoparticles. *Water* **2022**, *14*, 2301. [[CrossRef](#)]
11. Hayashi, N.; Kato, K.; Yamakata, A. Enhancement of photoelectrochemical activity of TiO_2 electrode by particulate/dense double-layer formation. *J. Chem. Phys.* **2020**, *152*, 241101. [[CrossRef](#)] [[PubMed](#)]
12. Chee, P.M.; Boix, P.P.; Ge, H.; Yanan, F.; Barber, J.; Wong, L.H. Core-Shell Hematite Nanorods: A Simple Method To Improve The Charge Transfer In The Photoanode For Photoelectrochemical Water-Splitting. *ACS Appl. Mater. Interf.* **2015**, *7*, 6852–6859.
13. Elbakkay, M.H.; El Roubay, W.M.A.; Marino-Lopez, A.; Sousa-Castillo, A.; Salgueirino, V.; El-Dek, S.I.; Farghali, A.A.; Correa-Duarte, M.A.; Millet, P. One-Pot Synthesis of $\text{TiO}_2/\text{Sb}_2\text{S}_3/\text{RGO}$ Complex Multicomponent Heterostructures For Highly Enhanced Photoelectrochemical Water Splitting. *Int. J. Hydrogen Energy* **2021**, *46*, 31216–31227. [[CrossRef](#)]
14. Ali, A.; Li, X.; Song, J.; Yang, S.; Zhang, W.; Zhang, Z.; Xia, R.; Zhu, L.; Xu, X. Nature-Mimic ZnO Nanoflowers Architecture: Chalcogenide Quantum Dots Coupling With $\text{ZnO}/\text{ZnTiO}_3$ Nanoheterostructures For Efficient Photoelectrochemical Water Splitting. *J. Phys. Chem. C* **2017**, *121*, 21096–21104. [[CrossRef](#)]
15. Suen, N.; Hung, S.; Quan, Q.; Zhang, N.; Xu, Y.; Chen, H.M. Electrocatalysis for the oxygen evolution reaction: Recent development and future perspectives. *Chem. Soc. Rev.* **2017**, *46*, 337–365. [[CrossRef](#)] [[PubMed](#)]
16. Lan, Y.; Liu, Z.; Guo, Z.; Li, X.; Zhao, L.; Zhan, L.; Zhang, M. A $\text{ZnO}/\text{ZnFe}_2\text{O}_4$ uniform core-shell heterojunction with a tubular structure modified by NiOOH for efficient photoelectrochemical water splitting. *Dalton Trans.* **2018**, *47*, 12181–12187. [[CrossRef](#)]
17. Kaushik, N.; Mohit, S.; Shaikh, M.M. Visible-Light-Induced Water Splitting Based on a Novel $\alpha\text{-Fe}_2\text{O}_3/\text{CdS}$ Heterostructure. *ACS Omega* **2017**, *2*, 3447–3456.
18. Miao, C.; Ji, S.; Xu, G.; Liu, G.; Ye, C. Micro-NanoStructured $\text{Fe}_2\text{O}_3:\text{Ti}/\text{ZnFe}_2\text{O}_4$ Heterojunction Films for Water Oxidation. *ACS Appl. Mater. Interfaces* **2012**, *4*, 4428–4433. [[CrossRef](#)] [[PubMed](#)]
19. Wang, Y.; Yu, T.; Chen, X.; Zhang, H.; Ouyang, S.; Li, Z.; Ye, J.; Zou, Z. Enhancement of Photoelectric Conversion Properties of $\text{SrTiO}_3/\alpha\text{-Fe}_2\text{O}_3$ Heterojunction Photoanode. *J. Phys. D Appl. Phys.* **2007**, *40*, 3925–3930.
20. Zhao, P.; Kronawitter, C.X.; Yang, X.; Fu, J.; Koel, B.E. $\text{WO}_3-\alpha\text{-Fe}_2\text{O}_3$ Composite Photoelectrodes with Low Onset Potential for Solar Water Oxidation. *Phys. Chem. Chem. Phys.* **2014**, *16*, 1327–1332. [[CrossRef](#)]
21. Chakraborty, M.; Roy, D.; Akash, S.; Thangavel, R. Post-treatment with ZnFe_2O_4 nanoparticles to improve photo-electrochemical performance of ZnO nanorods based photoelectrodes. *Solar Energy Mater. Solar Cells* **2019**, *200*, 109975. [[CrossRef](#)]
22. McDonald, K.J.; Choi, K.S. Synthesis and Photoelectrochemical Properties of $\text{Fe}_2\text{O}_3/\text{ZnFe}_2\text{O}_4$ Composite Photoanodes for Use in Solar Water Oxidation. *Chem. Mater.* **2011**, *23*, 4863–4869. [[CrossRef](#)]
23. Rashidi, M.; Ghasemi, F. Thermally oxidized MoS_2 -based hybrids as superior electrodes for supercapacitor and photoelectrochemical applications. *Electrochim. Acta* **2022**, *435*, 141379. [[CrossRef](#)]
24. Ghasemi, F.; Rashidi, M. Facile in situ fabrication of rGO/MoS_2 heterostructure decorated with gold nanoparticles with enhanced photoelectrochemical performance. *Appl. Surf. Sci.* **2021**, *570*, 151228. [[CrossRef](#)]